Diverse Influences of ENSO on the East Asian–Western Pacific Winter Climate Tied to Different ENSO Properties in CMIP5 Models

HAINAN GONG

Center for Monsoon System Research, Institute of Atmospheric Physics, Chinese Academy of Sciences, and University of Chinese Academy of Sciences, Beijing, China

LIN WANG, WEN CHEN, AND DEBASHIS NATH

Center for Monsoon System Research, Institute of Atmospheric Physics, Chinese Academy of Sciences, Beijing, China

GANG HUANG

State Key Laboratory of Numerical Modeling for Atmospheric Sciences and Geophysical Fluid Dynamics, Institute of Atmospheric Physics, Chinese Academy of Sciences, Beijing, China

WEICHEN TAO

Center for Monsoon System Research, Institute of Atmospheric Physics, Chinese Academy of Sciences, and University of Chinese Academy of Sciences, Beijing, China

ABSTRACT

The influence of El Niño–Southern Oscillation (ENSO) on the East Asian–western Pacific (EAWP) climate in boreal winter is investigated in the phase 5 of the Coupled Model Intercomparison Project (CMIP5) model results and then compared to that in the phase 3 (CMIP3) results. In particular, the role played by the differences among models in ENSO properties, including the amplitude and longitudinal extension of ENSO's sea surface temperature (SST) pattern, is analyzed. Results show that an eastward shrinking of ENSO's SST pattern leads to quite weak circulation and climatic responses over the EAWP regions in the models. On the contrary, a westward expansion of the SST pattern shifts the anomalous Walker circulation too far west. The resultant precipitation anomalies and lower-tropospheric atmospheric Rossby wave responses both extend unrealistically into the Indian Ocean, and the hemispheric asymmetry of the Rossby wave response is missing. All these features lead to unrealistic climatic impacts of ENSO over the EAWP regions. In contrast to the above two cases, a reasonable longitudinal extension of ENSO's SST pattern corresponds to better ENSO teleconnections over the EAWP regions. Nevertheless, the atmospheric responses over the western Pacific are still located farther west than observed, implying a common bias of CMIP5 models. In this case, a larger amplitude of ENSO variability to some extent helps to reduce model biases and facilitate better climatic responses to ENSO in the EAWP regions. Compared with CMIP3 models, CMIP5 models perform better in representing ENSO's impacts on the East Asian winter climate.

1. Introduction

El Niño–Southern Oscillation (ENSO) is a dominant interannual mode of climate variability that originates from ocean–atmosphere interactions in the tropical Pacific (Rasmusson and Carpenter 1982). Its basin-scale sea surface temperature (SST) anomalies not only induce significant changes in the tropical climate but also affect the extratropical climate through atmospheric teleconnections (e.g., Lau and Nath 1996; Trenberth et al. 1998). For example, ENSO can influence the climate of North America (Horel and Wallace 1981; Zhu et al. 2013), East Asia (Zhang et al. 1996; Chen et al. 2000; Wang et al. 2000), Oceania (Power et al. 1999; Cai et al. 2001), South Asia (Webster and Yang 1992), and

even Atlantic and Europe (Brönnimann 2007; Li and Lau 2012), and such impacts can be partly reproduced in numerical models (e.g., Catto et al. 2012; Weare 2013; Gong et al. 2014; Hurwitz et al. 2014; Lee et al. 2014).

The East Asian–western Pacific (EAWP) climate is significantly influenced by ENSO in boreal winter. The East Asian winter monsoon (EAWM) tends to be weak (strong) during El Niño (La Niña) winters, with widespread warming (cooling) and more (less) precipitation observed in subtropical East Asia (Li 1990; Chen et al. 2000; Wang and Feng 2011; Chen et al. 2013; Huang et al. 2012; J.-Y. Lee et al. 2013; Wang and Chen 2014). Although these climate anomalies are not exactly symmetric, they broadly have opposite signs in El Niño and La Niña winters (e.g., Zhang et al. 2015). The key system that realizes these impacts is an anomalous lower-tropospheric anticyclone or cyclone around the Philippine Sea (Wang et al. 2000) and the associated meridional wind anomalies along the coasts of East Asia (Zhang et al. 1996). This anomalous anticyclone (cyclone) is generated via the atmospheric Rossby wave response to the convective cooling (warming) anomalies around the western tropical Pacific associated with ENSO (Zhang et al. 1996; Wang et al. 2000; Feng et al. 2010), with additional contributions from the Indian Ocean SST (Watanabe and Jin 2002). In contrast to East Asia, Australia often experiences a warm (cool) and dry (wet) summer during the mature phase of El Niño (La Niña) in boreal winter (Power et al. 1999; Cai et al. 2010).

The influences of ENSO on the EAWP climate have been studied extensively for boreal summer (e.g., Huang and Wu 1989; Wang et al. 2003; Wu et al. 2009; Xie et al. 2009; Feng et al. 2011, 2014; J.-Y. Lee et al. 2011; S.-S. Lee et al. 2011; Yuan and Yang 2012), but less so for boreal winter, especially with numerical models. Coupled models may perform better than atmospheric general circulation models in simulating the teleconnection of ENSO over East Asia and the western Pacific in boreal winter (Jiang et al. 2013). Recently, the outputs from phase 5 of the Coupled Model Intercomparison Project (CMIP5) were released (Taylor et al. 2012). Compared with phase 3 (CMIP3) models, CMIP5 models have higher spatial resolutions and better representations of the Earth system. Based on 18 CMIP5 models, Gong et al. (2014) evaluated the influences of ENSO on the EAWM. They suggested that the representation of the ENSO–EAWM relationship in CMIP5 models depends on two key factors: the amplitude and the spatial structure of ENSO's SST pattern in the tropical central and eastern Pacific. However, some important issues remain open, such as whether the proposed two factors are sufficient for capturing the impacts of ENSO on the EAWP winter climate in CMIP5 models and what processes (if any) are responsible for the different climate impacts.

The present work is an extension of Gong et al. (2014) and aims to address the above two questions in detail. Here, 36 CMIP5 models are analyzed and briefly compared with 20 CMIP3 models. Section 2 describes the data and methodology, and section 3 groups the CMIP5 models according to ENSO properties. The ENSO teleconnection and its climatic impacts over East Asia and the western Pacific in boreal winter are discussed in section 4 using the CMIP5 model results and then briefly compared with CMIP3 model results in section 5. A summary of the key findings and further discussion are provided in section 6.

2. Data, model description, and analysis methods

a. Data

The SST data used in this study are from the monthly-mean Extended Reconstructed SST version 3 (ERSST. v3) dataset (Smith et al. 2008), which has a horizontal resolution of $2° \times 2°$ and covers the period from January 1854 to the present day. The observational proxies of monthly-mean atmospheric variables are from the 40-yr European Centre for Medium-Range Weather Forecasts Re-Analysis (ERA-40) dataset (Uppala et al. 2005), which spans the period September 1957–August 2002. The ERA-40 dataset has a horizontal resolution of $2.5° \times 2.5°$ and extends from 1000 to 1 hPa with 23 vertical pressure levels. The precipitation reconstruction (PREC) data from the National Oceanic and Atmospheric Administration (NOAA) are used as the global precipitation proxy (Chen et al. 2002). These data provide monthly precipitation anomalies in a $2.5° \times 2.5°$ grid starting from January 1948. In addition, the precipitation data from the monthly-mean Global Precipitation Climatology Project (GPCP) (Huffman et al. 2009) and Climate Prediction Center Merged Analysis of Precipitation (CMAP) (Xie and Arkin 1997) are also employed, which are both available in a $2.5° \times 2.5°$ grid since January 1979. Hereinafter, the results based on the above data are referred to as "observations."

b. Model description

Brief descriptions of the 36 CMIP5 and 20 CMIP3 models including their modeling centers and horizontal and vertical resolutions are listed in the appendix (Tables A1 and A2, respectively). In this study, the historical experiment was employed, and only one realization was analyzed for each model. To compare the model results with observations, the atmospheric variables and precipitation from model outputs have been bilinearly interpolated to a resolution of $2.5° \times 2.5°$, and the SST data from model outputs have been interpolated to a resolution of $2° \times 2°$.

TABLE 1. Number of CMIP5 models in each group according to F_{EXT} and F_{STD}.

	$F_{EXT} < 170°E$ (WE)	$170°E \leq F_{EXT} \leq 170°W$ (NE)	$F_{EXT} > 170°W$ (EE)
$F_{STD} > 1.2$ (LV)	7	3	0
$0.9 \leq F_{STD} \leq 1.2$ (NV)	3	3	4
$F_{STD} < 0.9$ (SV)	6	2	8

c. Analysis methods

Two types of ENSO were identified with different climate impacts (Ashok et al. 2007). In this study, the conventional ENSO is considered so that the Niño-3 index (i.e., area-averaged SST anomalies in 5°S–5°N, 150°–90°W) is used to measure the intensity of ENSO. The strength of the EAWM is represented by an index defined as the area-averaged 1000-hPa meridional winds along the east coast of China (10°–35°N, 115°–130°E) (Ji et al. 1997). The sign of the EAWM index is then reversed so that the positive (negative) index corresponds to strong (weak) EAWM. In Gong et al. (2014), the EAWM index defined on the basis of near-surface winds (Chen et al. 2000) was used, but the index on the basis of 1000-hPa winds is used here because the data for near-surface winds are not available in about half of the CMIP5 and CMIP3 models analyzed in this study. According to the assessment of Wang and Chen (2010), the representations of the EAWM's properties based on the two indices are quite similar. Regression of the normalized Niño-3 index is used to represent the anomalies associated with ENSO in boreal winter. Note that, in observations, both the teleconnection and the impact of El Niño on the EAWM are not exactly symmetric to those of La Niña because of the asymmetry of ENSO (e.g., Zhang et al. 2015). However, the CMIP5 models tend to produce much more symmetric features of ENSO compared with observations (Zhang and Sun 2014). Therefore, the linear regression method used here is mostly valid, although we need to keep in mind the asymmetric features of ENSO in reality.

The multimodel ensemble (MME) is calculated by simply averaging the variables over all the models with equal weighting. For example, the MME of a regression pattern is the average of all models' corresponding regression patterns. The confidence level is evaluated by a two-tailed Student's t test for each model. Where the confidence level of the MME is concerned, the t value of each model is first calculated and then averaged among all the models involved. The averaged t value is then used to evaluate the confidence level of the MME pattern. As shown in the following sections, the sample size of certain groups of models are sometimes small (Table 1), so the significance of regression patterns in the MME was also evaluated with the signal-to-noise ratio method

(Lee and Wang 2014), and almost the same results were obtained (not shown).

Unless explicitly stated, the analyses of observations and CMIP5 model results are for 1971–2000, which is the period when most of the high-quality data are available. Here, the 1971 winter refers to the 1970/71 winter. The analysis of CMIP3 model results is based on the period 1970–99 because of data availability. Because the PREC dataset covers the period 1971–2000 but only provides precipitation anomalies, the average of CMAP and GPCP precipitation in the period 1979–98 is used as the precipitation climatology to calculate the precipitation anomaly percentage. In this study, we focus on the interannual relationship. Therefore, all the original data are linearly detrended over the period 1971–2000 for observations and CMIP5 models and over the period 1970–99 for CMIP3 models. Winter means are constructed by averaging monthly-mean data of December–February (DJF).

3. Grouping CMIP5 models according to ENSO properties

In Gong et al. (2014), two factors were introduced to reflect the basic features of ENSO in CMIP5 models for boreal winter. One was the interannual standard deviation of the winter-mean Niño-3.4 index (F_{STD}) and the other was the number of grid points whose regressed winter-mean SST anomalies upon the simultaneous Niño-3.4 index exceed 0.6 K in the tropical central and eastern Pacific (8°S–8°N, 180°–110°W) (F_{GRIDS}). In this study, the Niño-3.4 index is replaced by the Niño-3 index to calculate F_{STD} because we focus on conventional ENSO. Accordingly, the area counting grids for F_{GRIDS} also needs to shift eastward, and is therefore modified to 8°S–8°N, 160°–85°W. Despite these differences between the present study and Gong et al. (2014), the main conclusions reported in the following sections are not affected (see section 6 for further discussion).

The correlation coefficient between the Niño-3 index and the EAWM index is -0.7 in observations, exceeding the 99% confidence level. Almost all the CMIP5 models capture this negative relation, despite being lower than observations, except CanCM4, MIROC-ESM, and MRI-CGCM3, which show weak positive correlations of 0.09, 0.07, and 0.05, respectively. Half (18 out of 36) of the CMIP5 models capture the strong link between the
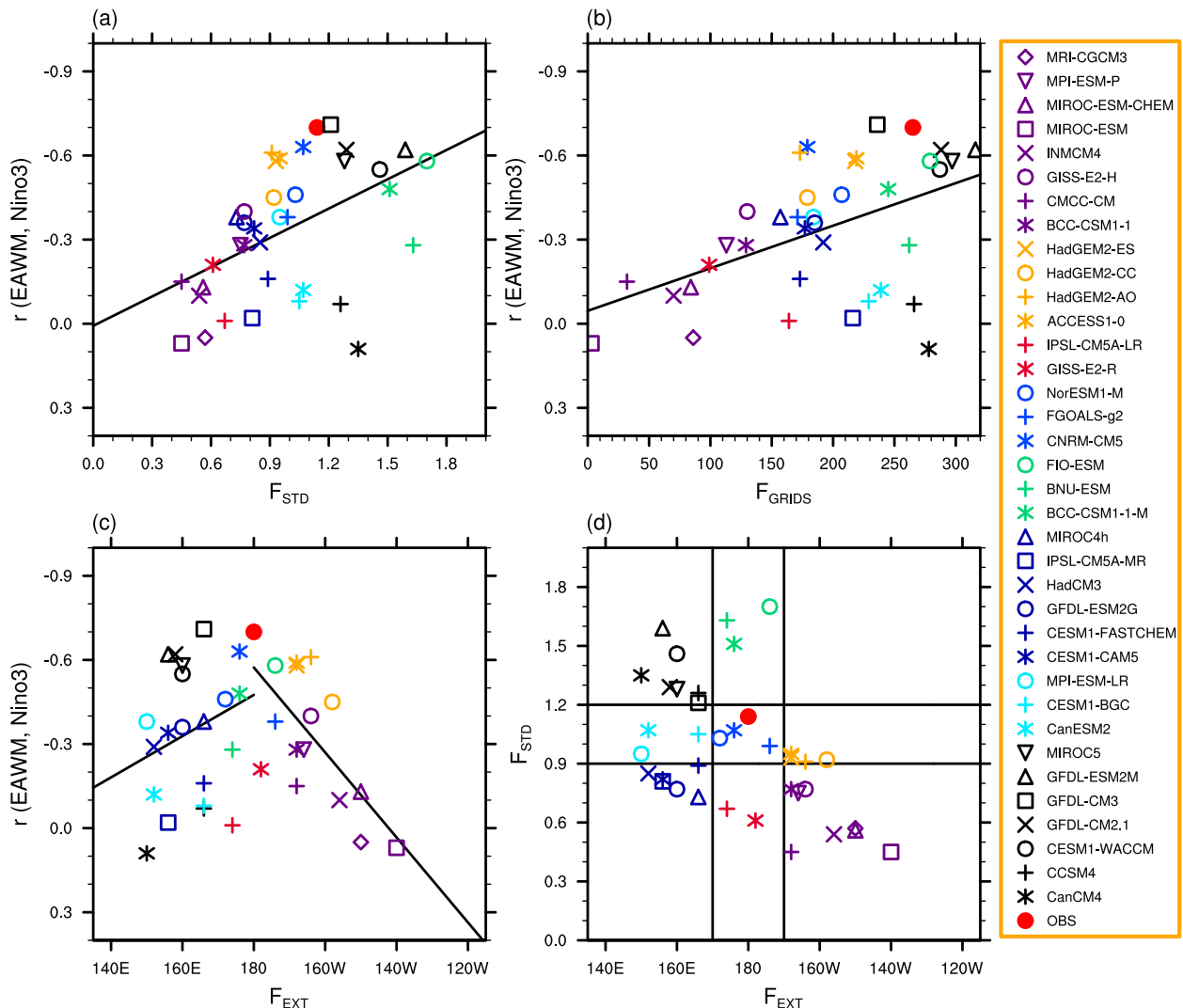
FIG. 1. Scatterplots of the correlation coefficient between the winter-mean Niño-3 and EAWM indices vs (a) F_{STD}, (b) F_{GRIDS}, and (c) F_{EXT} in 36 CMIP5 models. (d) Scatterplots of winter-mean F_{STD} vs F_{EXT} in 36 CMIP5 models. See text for the definition of F_{STD}, F_{GRIDS}, and F_{EXT}. Black lines in (a)–(c) denote linear fit.

Niño-3 and EAWM indices, with correlation coefficients exceeding the 95% confidence level. Figure 1a shows a scatter diagram in which the x and y axes represent F_{STD} and the correlation coefficient between the Niño-3 and EAWM indices, respectively, based on observations and 36 CMIP5 models. The figure reveals that larger ENSO variability (i.e., larger F_{STD}) tends to correspond to a better ENSO–EAWM relationship in most of the CMIP5 models. The correlation coefficient between the x and y variables is -0.49 (Fig. 1a), exceeding the 99% confidence level. When F_{STD} is replaced with F_{GRIDS}, a similar conclusion can be drawn: that is, a better ENSO pattern in the tropical eastern Pacific (i.e., larger F_{GRIDS}) tends to correspond to a closer ENSO–EAWM relationship, with the correlation coefficient also being

-0.49 (Fig. 1b). All these results are consistent with Gong et al. (2014), although more models were employed and slightly different definitions were used in F_{STD} and F_{GRIDS}.

It is important to note that the two factors (i.e., F_{STD} and F_{GRIDS}) to a large extent reflect the same properties of ENSO. For example, taking $F_{STD} > 0.9$ as the criterion, 20 out of 36 CMIP5 models are selected, and, taking $F_{GRIDS} > 178$ as the criterion, 21 are selected, among which 18 models are in both groups. In addition, the correlation coefficient between F_{STD} and F_{GRIDS} reaches as high as 0.9 in the 36 CMIP5 models. Therefore, the two factors could be simplified into one. Factor F_{STD} is employed because it is easy to calculate the standard deviation of the Niño-3 index. On the other

hand, a closer inspection reveals that, despite large F_{STD} and F_{GRIDS}, the ENSO–EAWM relationship is very weak in some models (e.g., in the bottom-right corner of Figs. 1a,b). This result suggests that the amplitude of ENSO variability alone may not be sufficient to explain the different ENSO–EAWM relationships among CMIP5 models and that other factors could be responsible. Recent studies suggest that the ENSO pattern often extends too far into the western Pacific in some CMIP5 models (Bellenger et al. 2014; Taschetto et al. 2014), which in turn modulates activities of convection and tropical cyclones over the western Pacific (Weller and Cai 2013). Meanwhile, our analysis also shows an excessive westward extension of ENSO's SST pattern in the models in the bottom-right corner of Figs. 1a,b (e.g., CanCM4 and CCSM4) compared with observations (not shown). Therefore, another important question is whether the longitudinal extension of ENSO's SST pattern could influence the relationship between ENSO and the winter-mean EAWP climate.

Based on the above consideration, a new factor that represents the longitudinal extension of ENSO's SST pattern (F_{EXT}) is defined as the western longitude of 0.6-K SST anomalies regressed upon the Niño-3 index at the equator in boreal winter. Figure 1c shows a scatter diagram in which the x and y axes represent F_{EXT} and the correlation coefficient between the Niño-3 and EAWM indices, respectively, based on observations and 36 CMIP5 models. The figure reveals that the observed F_{EXT} is 180° and that the closer the western longitude of the modeled ENSO pattern is to observations (red dot in Fig. 1c), the higher the ENSO–EAWM correlation is. This result is further confirmed by the correlation analysis with the absolute longitudinal difference between models and observations as one variable and the correlation coefficient between the Niño-3 and EAWM indices as the other variable. The correlation coefficient is 0.43 for the 36 CMIP5 models, exceeding the 95% confidence level. All these results suggest that the longitudinal extension of ENSO's SST pattern could indeed influence the ENSO teleconnection to the East Asian climate in CMIP5 models.

The correlation coefficient between F_{EXT} and F_{STD} is −0.4, exceeding the 95% confidence level. On one hand, this result indicates that a greater westward extension of ENSO's SST pattern broadly corresponds to larger ENSO variability; on the other hand, the relatively low correlation coefficient suggests that the two factors are to some extent independent of each other, which is confirmed by the fact that approximately half of the CMIP5 models with large westward F_{EXT} do not have large ENSO variability (Fig. 1d and Table 1). More importantly, F_{EXT} and F_{STD} are not necessarily related

because they reflect quite independent aspects of ENSO properties that do not have direct physical connection. Therefore, F_{EXT} can be employed as an independent factor to investigate the possible influence of ENSO properties on the EAWP winter climate.

Based on the longitudinal extension of ENSO's SST pattern (F_{EXT}), the 36 CMIP5 models are grouped into three categories: west extension (WE; $F_{EXT} < 170°$E), normal extension (NE; $170°$E $\leq F_{EXT} \leq 170°$W), and east extension (EE; $F_{EXT} > 170°$W).[1] Based on the amplitude of ENSO variability (F_{STD}), the 36 models can also be grouped into three categories: large variability (LV; $F_{STD} > 1.2$ K), normal variability (NV; 0.9 K $\leq F_{STD} \leq 1.2$ K), and small variability (SV; $F_{STD} < 0.9$ K).[2] A combination of the above two aspects results in nine groups (Table 1): WE+LV, WE+NV, WE+SV, NE+LV, NE+NV, NE+SV, EE+LV, EE+NV, and EE+SV. Note that none of the models fall into the EE+LV group. Therefore, in the following analysis, ENSO teleconnections in eight groups of CMIP5 models are investigated and compared with observations for boreal winter, where the ENSO teleconnection pattern is defined as the regression coefficients of a climatic variable onto the normalized Niño-3 index (Yang and DelSole 2012).

4. Teleconnections and climatic impacts of ENSO over the EAWP

a. Teleconnections

Figure 2a shows the observed winter-mean SST anomalies and 850-hPa wind anomalies associated with ENSO. Significant warm SST anomalies are observed in the tropical central and eastern Pacific, the tropical Indian Ocean, and along the east coast of East Asia, while cold SST anomalies are observed over the western North Pacific and subtropical Pacific. The resultant SST dipole with cold (warm) SST to the east (west) of the Philippines facilitates suppressed convection and diabatic cooling over

---

[1] We allow a buffer of 10° centered at the observed F_{EXT} (180°) to define the NE group. Almost identical results were obtained if the buffer was slightly wider (e.g., 12°; not shown). However, some results did not hold if the buffer was too narrow (e.g., 8°; not shown), likely because of the resultant small sample of the NE group.

[2] The observed F_{STD} is 1.14 K, while two-thirds of the models underestimate this value with the MME of all F_{STD} being 0.96 K. Therefore, we take the average of the two values (i.e., 1.05 K) as the base point and allow a buffer of 0.15 K to define the NV group. Almost identical results were obtained if a wider buffer (e.g., 0.2 K) was used or the observed F_{STD} was used as the base point (not shown). However, some results did not hold if the buffer was too narrow (e.g., 0.1 K; not shown), likely because of the resultant small sample of the NV group.
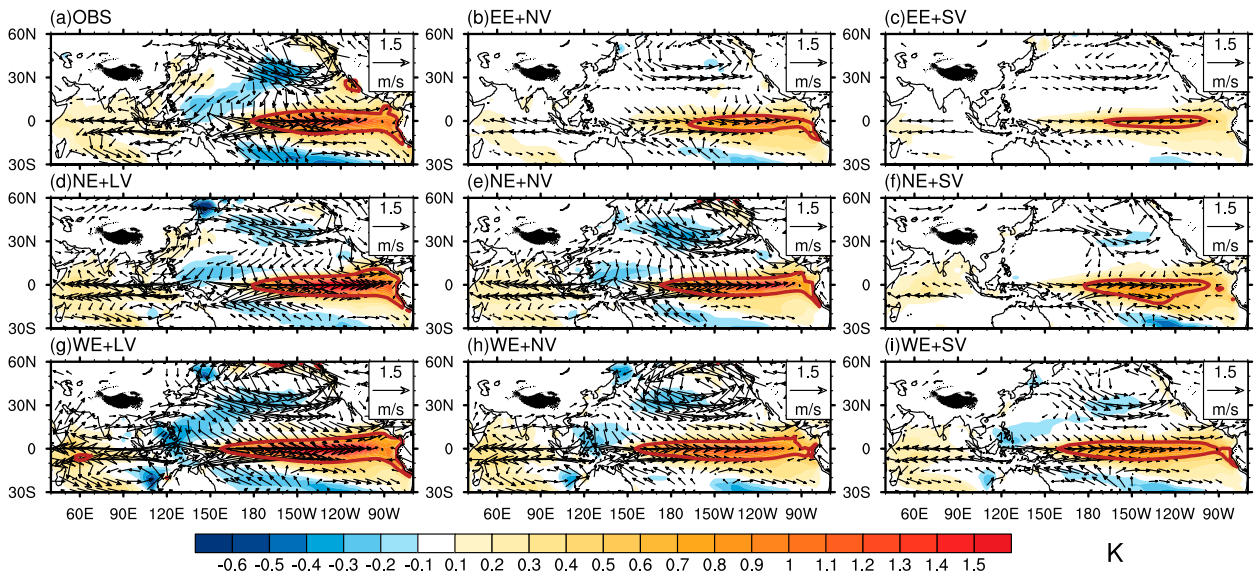
FIG. 2. (a) Regressed anomalies of winter-mean SST (shading) and 850-hPa winds (vectors) upon the simultaneous normalized Niño-3 index in observations. (b)–(i) As in (a), but for the MME of regressed anomalies in the eight groups of CMIP5 models. Only values exceeding the 90% confidence level are shown. Thick red solid contours denote the 0.6-K profiles of ENSO's regressed SST patterns in observations and the eight groups. See text or Table 1 for a definition of the groups and section 2c for the procedures used to derive the figures.

the tropical western Pacific. This convective cooling excites an atmospheric Rossby wave response and forms an anomalous anticyclone in the lower troposphere around the Philippines (Zhang et al. 1996), which is the key system through which ENSO influences the East Asian winter climate, known as the Pacific–East Asia teleconnection (Wang et al. 2000). In the Southern Hemisphere, an anomalous lower-tropospheric anticyclone is observed to the west of Australia, which is one of the key systems through which ENSO influences the Australian summer climate (e.g., Wang et al. 2003; Cai et al. 2010).

The warm SST in the tropical Pacific and Indian Ocean can be reproduced, albeit with different strength, in all the eight groups of CMIP5 models (Figs. 2b–i), while the cold SST in the western North Pacific is very weak in the EE group (Figs. 2b,c). Accordingly, the 850-hPa wind responses (Figs. 2b,c) and precipitation anomalies (not shown) over the western Pacific are very weak in the EE group because of the insufficient strength of anomalous SST and the resultant convective cooling. On the other hand, the 850-hPa wind responses over the western Pacific are also very weak in the NE+SV and WE+SV groups (Figs. 2f,i). Although the SST patterns in the two groups are more reasonable than those in the EE group, the small variability of ENSO is not strong enough to induce a precipitation change and excite a Rossby wave response over the western North Pacific (Gong et al. 2014). For the remaining four groups (NE+LV, NE+NV, WE+LV, and WE+NV), the SST and wind anomalies have

comparable magnitude to observations over the western Pacific (Figs. 2d,e,g,h). Therefore, these four groups are examined in detail in the following part of this paper.

In the NE+LV and NE+NV groups, the ENSO-related SST pattern is captured well, with a reasonable longitudinal extent of warm SST anomalies in the tropical Pacific and warm (cold) SST anomalies to the west (east) of the Philippines (Figs. 2d,e). Accordingly, an anomalous lower-tropospheric anticyclone that resembles observations is observed around the Philippines, with significant southwesterly wind anomalies present over the South China Sea and along the coast of East Asia. In the Southern Hemisphere, a zonally elongated anticyclone is observed to the west of Australia, quite similar to observations. The SST pattern and 850-hPa wind anomalies show better resemblance to observations in the NE+LV group (Fig. 2d) than in the NE+NV group (Fig. 2e), implying that larger ENSO variability tends to facilitate better teleconnection over the western Pacific when the western extension of ENSO's SST pattern is close to observations.

In contrast, in the WE+LV and WE+NV groups the SST pattern in the tropical region is shifted westward compared with observations. Cold SST anomalies occupy the South China Sea and even the Bay of Bengal part of the northern Indian Ocean, where in reality there should be warm SST (Figs. 2g,h). Consequently, the anomalous lower-tropospheric anticyclone shifts westward, and the South China Sea is occupied by northerly wind anomalies, opposite to observations (Figs. 2g,h). In addition,
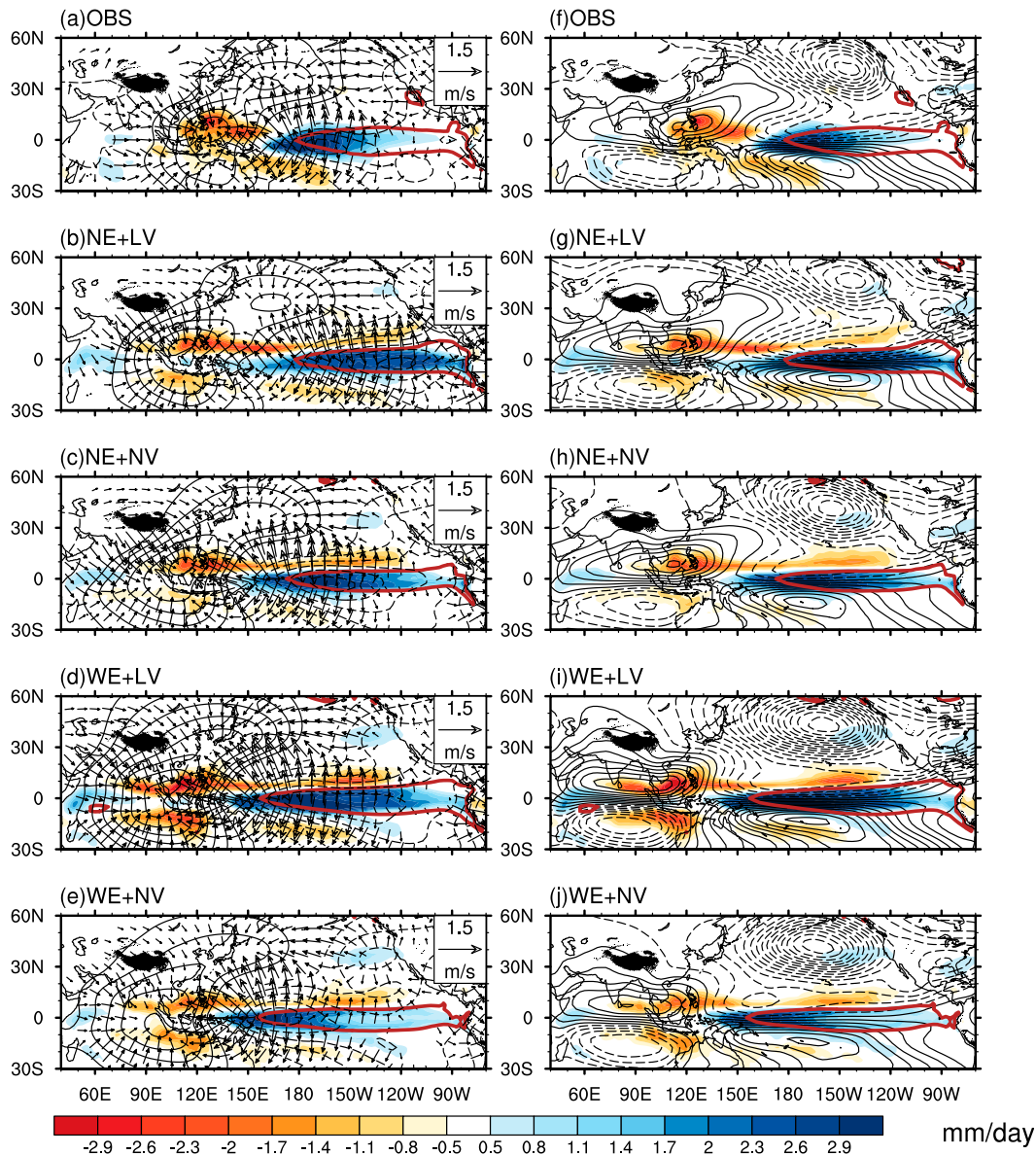
Precip & 200hPa VP
Precip & 850hPa SF

FIG. 3. (a) Regressed anomalies of winter-mean precipitation (shading), 200-hPa velocity potential (contours), and 200-hPa divergent winds (vectors) onto the simultaneous normalized Niño-3 index in observations. (b)–(e) As in (a), but for the MME of regressed anomalies in the (b) NE+LV group, (c) NE+NV group, (d) WE+LV group, and (e) WE+NV group. (f)–(j) As in (a)–(e), but for precipitation (shading) and 850-hPa streamfunction (contours). Only values exceeding the 90% confidence level are shown. Thick red solid contours denote the 0.6-K profiles of ENSO's regressed SST patterns in observations and the four groups. Contour intervals are $0.4 \times 10^6\,\mathrm{m^2\,s^{-1}}$ in (a)–(e) and $0.3 \times 10^6\,\mathrm{m^2\,s^{-1}}$ in (f)–(j). See text or Table 1 for a definition of the groups and section 2c for the procedures used to derive the figures.

excessively cold SST anomalies are observed along the west coast of Australia, and the accompanying anticyclone is also shifted slightly westward. All these results suggest that the excessive westward extension of ENSO's SST pattern leads to an unrealistic westward shift of lower-tropospheric wind anomalies.

To further understand the atmospheric responses to these different SST configurations, the divergent and rotational circulations as well as precipitation are examined (Fig. 3). During the mature phase of warm ENSO, the observed 200-hPa velocity potential shows anomalous divergence to the east of 180°, convergence

over the Maritime Continent centered to the east of the Philippines at about 8°N, and a secondary convergence center to the east of Japan (Fig. 3a). The resultant anomalous ascending motion over the tropical central and eastern Pacific facilitates more precipitation, while the anomalous descending motion over the tropical western Pacific favors less precipitation (Fig. 3a). The centers of the precipitation anomalies coincide nicely with the centers of upper-level convergence and divergence. As a result, the suppressed precipitation and diabatic heating excite a direct Rossby wave response (Zhang et al. 1996; Wang et al. 2000; Feng et al. 2010) and trigger a pair of lower-tropospheric off-equatorial anomalous anticyclones over the western North Pacific and southern Indian Ocean (Fig. 3f), respectively.

In the four groups of CMIP5 models, the pattern of tropical precipitation is roughly reproduced (Figs. 3b–e,g–j) and generally follows that of SST (Figs. 2d,e,g,h). There are two common biases of precipitation in the four groups. One is the enhanced precipitation belt along the equator over the Maritime Continent, which seems to be a common bias in most coupled general circulation models, arising from the air–sea interactions via Bjerknes feedback (Li and Xie 2014). The other is the westward-extended (eastward-extended) off-equatorial belt of suppressed precipitation over the northern and southern Indian Ocean (tropical Pacific along ~10°N), which seems to be the embodiment of the double ITCZ problem in the anomalous precipitation field.

In response to the precipitation anomalies, the upper-tropospheric divergent circulation can be broadly reproduced in the four groups of models (Figs. 3b–e). It is noteworthy that the center of the anomalous velocity potential around the Maritime Continent is located at least 10° farther west than in observations, even in the NE+LV and NE+NV groups, which reproduce reasonable westward extension of ENSO's SST pattern (Figs. 3b,c). This bias, which is more severe in the WE+LV and WE+NV groups (Figs. 3d,e), is coupled with unrealistic westward-extended off-equatorial belts of suppressed precipitation over the South China Sea and eastern Indian Ocean, indicating a possible origin from precipitation biases. As a result, the Rossby wave responses in the lower troposphere shift westward, especially in the Northern Hemisphere. The center of the anticyclone around the Philippines is located over the South China Sea in the NE+LV and NE+NV groups, which is roughly similar to observations (Figs. 3g,h), while it is located over the northern Indian Ocean in the WE+LV and WE+NV groups, which is quite different from observations (Figs. 3i,j). The convergence center to the east of Japan (Fig. 3a) is captured well in the NE+LV and NE+NV groups (Figs. 3b,c) but is shifted

westward from Japan in the WE+LV and WE+NV groups (Figs. 3d,e).

Another important feature of the atmospheric response to ENSO over the western Pacific is its asymmetry about the equator arising from topography and the configurations of the basic wind field (Wang et al. 2003). The observed velocity potential and precipitation anomalies are much stronger over the western North Pacific than over the western South Pacific (Fig. 3a); hence, the lower-tropospheric anticyclone in the western North Pacific is stronger than its counterpart in the Southern Hemisphere (Fig. 3f). This feature is successfully captured in the NE+LV and NE+NV groups, especially in the NE+LV group (Figs. 3b,c,g,h), whereas it is poorly reproduced in the WE+LV and WE+NV groups (Figs. 3d,e,i,j). The poor performance in the latter two groups could be attributable to the homogeneous lower boundary and the biased symmetric precipitation anomalies over the Indian Ocean where the descending branch of anomalous Walker circulation is located as a result of the excessive westward extension of ENSO's SST pattern.

b. Climatic impacts on East Asia and Australia

During the mature phase of El Niño, warm anomalies are observed along the coasts of East Asia and over the Maritime Continent and Australia (Fig. 4a), facilitating a weak EAWM (Li 1990; Chen et al. 2000) and hot Australian summer monsoon (Jeong et al. 2012). This feature is best reproduced in the NE+LV group, albeit with an unrealistic warming that is much stronger than observations over the Siberian high regions (Fig. 4b). In the NE+NV group, the warm anomalies along the coast of East Asia are much weaker than those in observations, and slightly weak cold anomalies are observed over northern China (Fig. 4c). This difference indicates that, when the westward extension of ENSO's SST pattern is reasonable, large ENSO variability may help to form a more reasonable temperature response along the coast of East Asia and over the western Pacific. In the WE+LV and WE+NV groups, the temperature responses resemble that in the NE+NV group over East Asia, but the unrealistic cooling over northern China and along the coastal seas is much more evident. Note that the observed surface air temperature anomalies are weak and insignificant over East Asia, although the East Asian monsoon is weak in El Niño winters (Fig. 4a). However, all the CMIP5 models significantly exaggerate these temperature anomalies over East Asia (Figs. 4b–e). In the Southern Hemisphere, the warm anomalies in Australia show a similar pattern to observations, while the magnitudes of anomalies are much larger in the four groups than in observations and

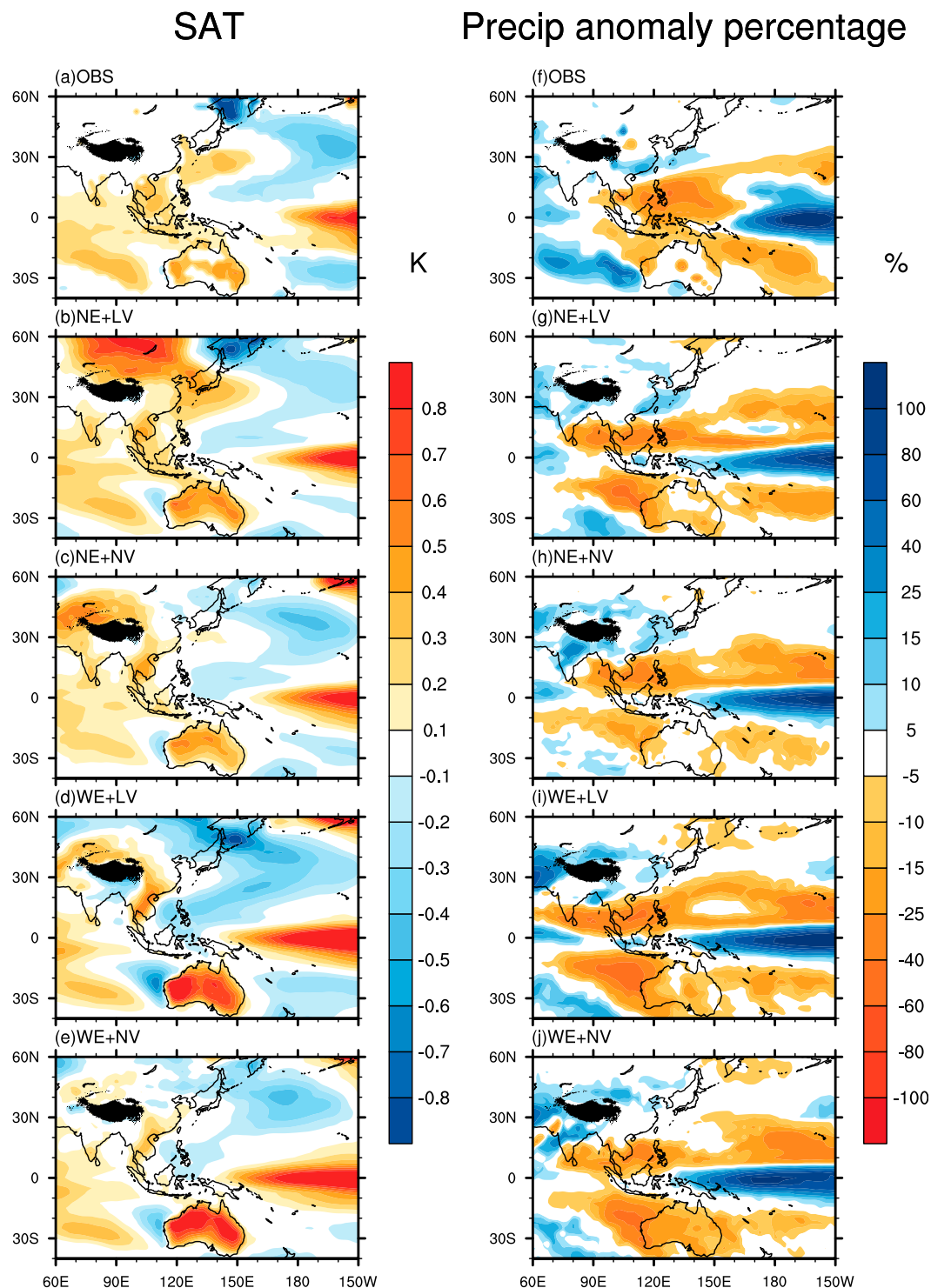## SAT

Precip anomaly percentage

FIG. 4. (a) Regressed anomalies of winter-mean surface air temperature onto the simultaneous normalized Niño-3 index in observations. (b)–(e) As in (a), but for the MME of regressed anomalies in the (b) NE+LV group, (c) NE+NV group, (d) WE+LV group, and (e) WE+NV group. (f)–(j) As in (a)–(e), but for the precipitation anomaly percentage. Only values exceeding the 90% confidence level are shown. See text or Table 1 for a definition of the groups and section 2c for the procedures used to derive the figures.

TABLE 2. RMSEs of the correlation coefficient between the Niño-3 and EAWM indices in CMIP5 and CMIP3 models based on all models and a model sample that only consists of NE models. The number of models used to calculate the RMSE is indicated in parentheses.

	CMIP5 (36/8)	CMIP3 (20/4)
RMSE (all models/NE only)	0.440/0.374	0.556/0.401

the problem is more severe in the WE+LV and WE+NV groups (Figs. 4b–e).

Figures 4f–j show the ENSO-related precipitation anomaly percentage: that is, precipitation anomalies (PREC data) normalized by their climatology (1979–98; average of GPCP and CMAP data). In boreal winter of El Niño, enhanced precipitation is observed over a band stretching from southern China to south of Japan and suppressed precipitation is observed around the Philippines, over the Maritime Continent, and along the northern coast of Australia (Zhang and Sumi 2002; Cai et al. 2010; Feng et al. 2010; Wang and Feng 2011) (Fig. 4f). In CMIP5 models, the enhanced subtropical precipitation belt over East Asia is captured well in the NE+LV and NE+NV groups, with reasonable location and magnitude (Figs. 4g,h) due to the well-simulated Philippine anticyclone (Figs. 2d,e). In contrast, the location of this precipitation belt is located too far north in the WE+LV and WE+NV groups (Figs. 4i,j) because of the northward extension of the northern edge of the anomalous anticyclone (Figs. 2g,h). Besides, the magnitude of anomalies along the shifted precipitation belt is weaker than in observations. In Australia, the suppressed precipitation is also captured better in the two NE groups than the two WE groups (Figs. 4g–j), consistent with the simulation of higher temperature (Figs. 4b–e).

The above results suggest that the excessive westward extension or eastward shrinking of ENSO's SST pattern could lead to an unrealistic response of surface air temperature and precipitation over East Asian and western Pacific regions. To further reveal this effect, we separately calculate the root-mean-square error (RMSE) of the correlation coefficient between the Niño-3 and EAWM indices on the basis of all the models, and the models in the NE group only. The RMSE of the correlation coefficient is reduced from 0.440 to 0.374 (by 15%) if only the NE group is considered (Table 2). This result confirms that the longitudinal extension of ENSO's SST pattern in CMIP5 models can indeed exert strong impacts on the relationship between ENSO and the EAWP climate in boreal winter by modulating the Walker circulation and related atmospheric responses over the western Pacific.

5. Comparison with CMIP3 models

The question naturally arises as to whether the above conclusion for CMIP5 models is also applicable to CMIP3 models. To address this, we briefly examine the issue in 20 CMIP3 models, focusing on East Asia. A scatter diagram between F_{EXT} and F_{STD} indicates that a larger westward extension of ENSO's SST pattern generally corresponds to larger ENSO variability in CMIP3 models (Fig. 5a). Nevertheless, the correlation coefficient between the two is only -0.31, suggesting that F_{EXT} and F_{STD} can to a large extent be regarded as two independent factors. This is similar to the situation in CMIP5 models.

Figure 5b shows a scatter diagram in which the x and y axes represent F_{EXT} and the correlation coefficient between the Niño-3 and EAWM indices, respectively. There is a tendency that the closer the western longitude of the modeled ENSO pattern is to observations, the tighter the ENSO–EAWM relationship. Taking the same criteria of F_{EXT} to define the NE group, the RMSE of the y-axis variable (i.e., the correlation coefficient between the Niño-3 and EAWM indices) is separately examined on the basis of all the models, and the models in the NE group only. The RMSE of the correlation coefficient is reduced from 0.556 to 0.401 (by 28%) if only the NE group is considered (Table 2), suggesting that a more reasonable longitudinal extension of ENSO's SST pattern in CMIP3 models could better represent the ENSO–EAWM relationship in boreal winter. Figure 5c shows a scatter diagram in which the x and y axes represent F_{STD} and the correlation coefficients between the Niño-3 and EAWM indices, respectively, based on observations and 20 CMIP3 models. The correlation coefficient between the x- and y-axis variables is -0.62, exceeding the 99% confidence level (Fig. 5c). This relationship suggests that, in general, larger ENSO variability (i.e., F_{STD}) also corresponds to a better ENSO–EAWM relationship. All these results are consistent with those in CMIP5 models.

It is also important to note that the RMSE in CMIP5 models is smaller than that in CMIP3 models (Table 2). This conclusion holds when all models are considered (0.440 versus 0.556), and when models in the NE groups only are considered (0.374 versus 0.401). The difference between the two RMSEs is 26.4% and 7.2% for the two situations, respectively. The clear reduction of RMSE, especially when all models are considered, suggests that overall there is a significant improvement in representing the link between ENSO and EAWM in CMIP5 models compared with CMIP3 models.

6. Summary and discussion

In this study, the ENSO teleconnection and its impacts on the EAWP climate in boreal winter are
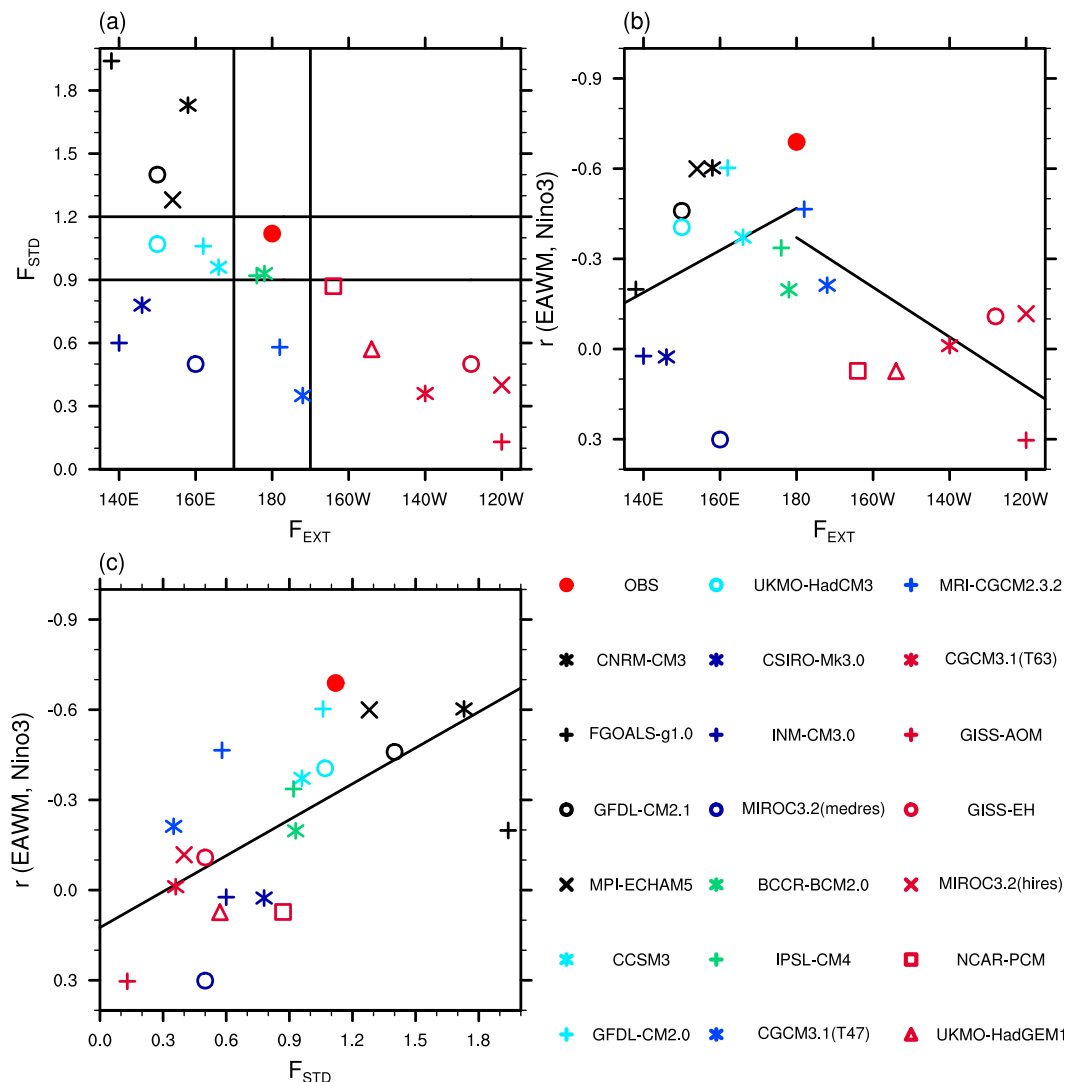
FIG. 5. (a)–(c) As in Figs. 1d,c,a, but based on 20 CMIP3 models.

investigated in 36 CMIP5 models and briefly compared with those in 20 CMIP3 models. Overall, the significant relationship between ENSO and EAWM, measured by the correlation coefficient between the Niño-3 and EAWM indices, can be captured by half of the 36 CMIP5 models. This relationship is better reproduced if the amplitude of ENSO variability (F_{STD}) is larger than observed or when the longitudinal extent of ENSO's SST pattern (F_{EXT}) is closer to observations. Meanwhile, our analysis suggests that a large amplitude of ENSO variability generally corresponds to a westward extension of ENSO's SST pattern, but the two factors (i.e., F_{STD} and F_{EXT}) are to a large extent independent of each other. Therefore, F_{STD} and F_{EXT} are employed as two independent criteria to divide the 36 CMIP5 models into 9 groups to further investigate the

dependence of ENSO teleconnection and its climatic impacts over the EAWP region upon the amplitude of ENSO variability and longitudinal extension of ENSO's SST pattern.

Analysis of CMIP5 models suggests that the ENSO teleconnection to East Asia and the western Pacific is very weak when ENSO variability is small or ENSO's SST pattern is too confined in the tropical eastern Pacific. In contrast, the ENSO teleconnections are strong but shifted too far west if the ENSO's SST pattern is located too far west with reasonable amplitude of variability. The descending branch of anomalous Walker circulation and the resultant lower-tropospheric off-equatorial anticyclones shift from the western North Pacific into the northern Indian Ocean. Therefore, unrealistic temperature and precipitation anomalies are observed over East Asia and
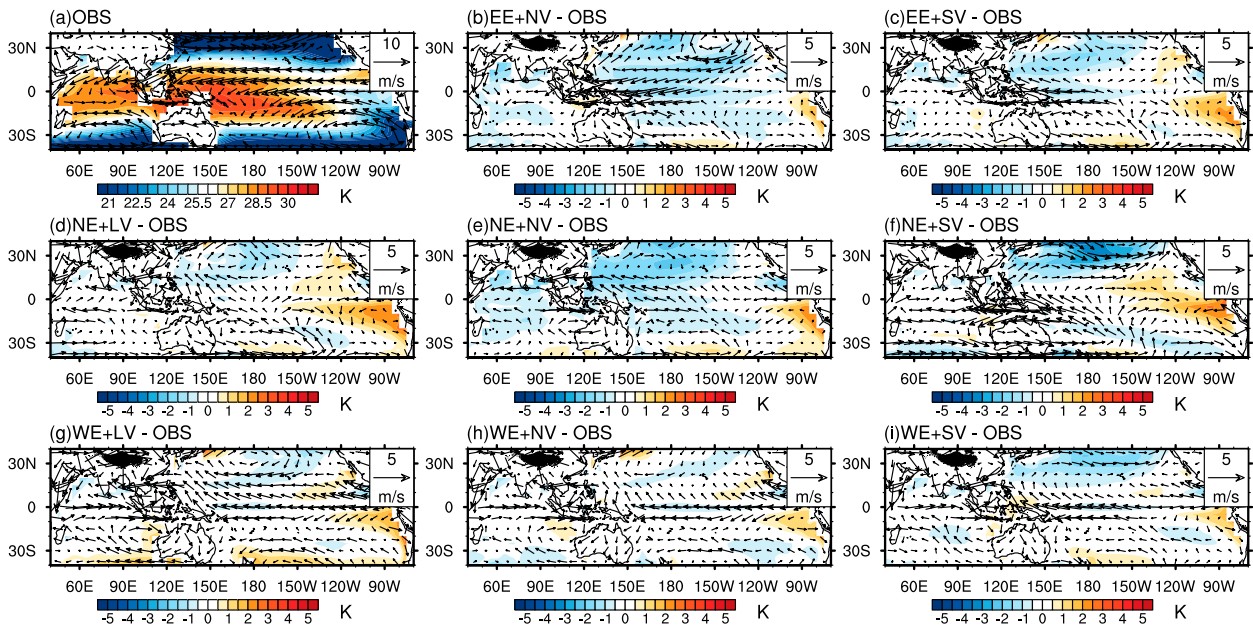
FIG. 6. (a) The climatology of winter-mean SST (shading) and 850-hPa winds (vectors) in observations based on the period 1971–2000. (b)–(i) The difference of the climatology between the MME of CMIP5 models in each group and observations. See text or Table 1 for a definition of the groups and section 2c for the procedures used to derive the figures.

Australia. On the other hand, the ENSO teleconnections still show a slight westward shift even if the longitudinal extension of ENSO's SST pattern is in a reasonable range, which seems to be a common bias in CMIP5 models. In this case, excessive ENSO variability would significantly improve the performance of ENSO's impacts on the EAWP climate. In CMIP3 models, the amplitude of ENSO variability and longitudinal extension of ENSO's SST pattern can also modulate ENSO's impacts on the EAWP climate, similar to CMIP5 models. Compared with CMIP3 models, CMIP5 models show clear improvement in representing the ENSO–EAWM relationship, although the source of this improvement may be very complex.

An unrealistic longitudinal extent of ENSO's SST pattern is a common bias in coupled general circulation models (T. Lee et al. 2013) and may be partly caused by the inability of models to simulate the mean state of SST, the climatological trade winds over the tropical and subtropical Pacific, and the resultant air–sea interactions via Bjerknes feedback (Kim et al. 2014; Magnusson et al. 2013; Li and Xie 2014). Figure 6 shows the observed climatology of winter-mean SST and 850-hPa winds together with their corresponding model biases in the eight groups. Clear easterly biases are observed in all groups of models over the tropical western and central Pacific (Figs. 6b–i). In particular, the easterly bias can extend to the tropical eastern Pacific in the WE groups (Figs. 6g–i). This result implies that the model biases in the basic state

may correspond to biases in the mode of interannual variability. For example, the excessive westward extension of ENSO's SST pattern might be related to the surface easterly biases of model climatology in the tropical eastern Pacific, whereas surface easterly biases confined in the tropical western and central Pacific alone might be unable to result in the westward extension of ENSO's SST pattern. Given its significant influences on the western Pacific winter climate, the longitudinal extent of ENSO's SST pattern may need to be taken into account when making projections of future climate for the EAWP regions. On the other hand, although the importance of the longitudinal extent of ENSO's SST pattern for ENSO teleconnection and climatic impacts is suggested in this study, there remains the possibility that other properties of ENSO such as the meridional width of the ENSO pattern (Zhang et al. 2013; Zhang and Jin 2012) may also be influential, and these need to be investigated in the future.

In this study, the Niño-3 index is used to define ENSO. In fact, the analyses were also repeated with the Niño-3.4 index and almost the same results were obtained (not shown). This is because the correlation coefficients between the Niño-3 and Niño-3.4 indices exceed 0.95 in 34 out of the 36 CMIP5 models. Therefore, the categorization of models remains almost the same if the Niño-3 index is replaced by the Niño-3.4 index, implying a relative insensitivity of our results to the choice of ENSO index. On the other hand, the observed El Niño and La

TABLE A1. The climate modeling centers and CMIP5 models used in this study: The horizontal resolution and vertical levels of each model are also listed.

Model	Center	Atmospheric resolution
ACCESS1.0	Commonwealth Scientific and Industrial Research Organisation (CSIRO) and Bureau of Meteorology (BOM), Australia	192×144, L38
BCC_CSM1.1	Beijing Climate Center, China Meteorological Administration	128×64, L26
BCC_CSM1.1(m)	Beijing Climate Center, China Meteorological Administration	320×160, L26
BNU-ESM	College of Global Change and Earth System Science, Beijing Normal University	128×64, L26
CanCM4	Canadian Centre for Climate Modelling and Analysis	128×64, L35
CanESM2	Canadian Centre for Climate Modelling and Analysis	128×64, L35
CCSM4	National Center for Atmospheric Research	288×192, L26
CESM1(BGC)	Community Earth System Model contributors	288×192, L26
CESM1(CAM5)	Community Earth System Model contributors	288×192, L30
CESM1(FASTCHEM)	Community Earth System Model contributors	288×192, L26
CESM1(WACCM)	Community Earth System Model contributors	144×96, L66
CMCC-CM	Centro Euro-Mediterraneo per I Cambiamenti Climatici	480×240, L31
CNRM-CM5	Centre National de Recherches Météorologiques/Centre Européen de Recherche et Formation Avancée en Calcul Scientifique	256×128, L31
FGOALS-g2	LASG, Institute of Atmospheric Physics, Chinese Academy of Sciences and CESS, Tsinghua University	128×60, L26
FIO-ESM	First Institute of Oceanography, State Oceanic Administration (SOA), China	128×64, L26
GFDL CM2.1	NOAA/Geophysical Fluid Dynamics Laboratory	144×90, L24
GFDL CM3	NOAA/Geophysical Fluid Dynamics Laboratory	144×90, L48
GFDL-ESM2G	NOAA/Geophysical Fluid Dynamics Laboratory	144×90, L24
GFDL-ESM2M	NOAA/Geophysical Fluid Dynamics Laboratory	144×90, L24
GISS-E2-H	NASA Goddard Institute for Space Studies	144×90, L40
GISS-E2-R	NASA Goddard Institute for Space Studies	144×90, L40
HadCM3	Met Office Hadley Centre	96×73, L19
HadGEM2-AO	National Institute of Meteorological Research/Korea Meteorological Administration	192×144, L38
HadGEM2-CC	Met Office Hadley Centre	192×144, L60
HadGEM2-ES	Met Office Hadley Centre (additional HadGEM2-ES realizations contributed by Instituto Nacional de Pesquisas Espaciais)	192×144, L38
INM-CM4	Institute of Numerical Mathematics	180×120, L21
IPSL-CM5A-LR	L'Institute Pierre-Simon Laplace	96×96, L39
IPSL-CM5A-MR	L'Institute Pierre-Simon Laplace	144×143, L39
MIROC4h	Atmosphere and Ocean Research Institute (University of Tokyo), National Institute for Environmental Studies, and Japan Agency for Marine-Earth Science and Technology	640×320, L56
MIROC5	Atmosphere and Ocean Research Institute (University of Tokyo), National Institute for Environmental Studies, and Japan Agency for Marine-Earth Science and Technology	256×128, L40
MIROC-ESM	Japan Agency for Marine-Earth Science and Technology, Atmosphere and Ocean Research Institute (University of Tokyo), and National Institute for Environmental Studies	128×64, L80
MIROC-ESM-CHEM	Japan Agency for Marine-Earth Science and Technology, Atmosphere and Ocean Research Institute (University of Tokyo), and National Institute for Environmental Studies	128×64, L80
MPI-ESM-LR	Max Planck Institute for Meteorology	192×96, L47
MPI-ESM-P	Max Planck Institute for Meteorology	192×96, L47
MRI-CGCM3	Meteorological Research Institute	320×160, L48
NorESM1-M	Norwegian Climate Centre	144×96, L26

Niña are asymmetric in both their structures and associated climatic anomalies (e.g., Zhang et al. 2015). Therefore, the current results derived from linear regression were also compared with those derived from composite analysis in El Niño and La Niña winters. The comparison revealed that a considerable part of the features of El Niño and La Niña in CMIP5 models can be captured by the linear regression method (not shown), because CMIP5 models tend to produce a symmetric ENSO (Zhang and Sun 2014).

TABLE A2. The climate modeling centers and CMIP3 models used in this study: The horizontal resolution and vertical levels of each model are also listed.

Model	Center	Atmospheric resolution
BCCR-BCM2.0	Bjerknes Centre for Climate Research, Norway	128×64, L31
CGCM3.1(T47)	Canadian Centre for Climate Modelling and Analysis, Canada	96×48, L29
CGCM3.1(T63)	Canadian Centre for Climate Modelling and Analysis, Canada	128×64, L31
CCSM3	National Center for Atmospheric Research, United States	128×64, L26
CNRM-CM3	Centre National de Recherches Meteorologiques, France	128×64, L45
CSIRO Mk3.0	Australia's Commonwealth Scientific and Industrial Research Organisation, Australia	96×196, L18
ECHAM5	Max Planck Institute for Meteorology, Germany	192×96, L31
FGOALS-g1.0	Institute of Atmospheric Physics, China	128×60, L26
GFDL CM2.0	Geophysical Fluid Dynamics Laboratory, United States	144×90, L24
GFDL CM2.1	Geophysical Fluid Dynamics Laboratory, United States	144×90, L24
GFDL CM2.0	NASA Goddard Institute for Space Studies, United States	90×60, L12
GISS-EH	NASA Goddard Institute for Space Studies, United States	72×46, L20
HadCM3	Met Office Hadley Centre, United Kingdom	96×73, L19
HadGEM1	Met Office Hadley Centre, United Kingdom	192×145, L38
INM-CM3.0	Institute of Numerical Mathematics, Russia	72×45, L21
IPSL-CM4	L'Institut Pierre-Simon Laplace, France	96×72, L19
MIROC3.2(hires)	Center for Climate System Research, Tokyo, Japan	320×160, L56
MIROC3.2(medres)	Center for Climate System Research, Tokyo, Japan	128×64, L20
MRI-CGCM2.3.2	Meteorological Research Institute, Japan	128×64, L30
PCM	National Center for Atmospheric Research, United States	128×64, L26

APPENDIX

Information of Models

The climate modeling centers and models used in this study are described in Tables A1 and A2. Expansions of model name acronyms are available at http://www.ametsoc.org/PubsAcronymList.

REFERENCES

Ashok, K., S. K. Behera, S. A. Rao, H. Weng, and T. Yamagata, 2007: El Niño Modoki and its possible teleconnection. *J. Geophys. Res.,* **112,** C11007, doi:10.1029/2006JC003798.

Bellenger, H., E. Guilyardi, J. Leloup, M. Lengaigne, and J. Vialard, 2014: ENSO representation in climate models: From CMIP3 to CMIP5. *Climate Dyn.,* **42,** 1999–2018, doi:10.1007/s00382-013-1783-z.

Brönnimann, S., 2007: Impact of El Niño–Southern Oscillation on European climate. *Rev. Geophys.,* **45,** RG3003, doi:10.1029/2006RG000199.

Cai, W., P. H. Whetton, and A. B. Pittock, 2001: Fluctuations of the relationship between ENSO and northeast Australian rainfall. *Climate Dyn.,* **17,** 421–432, doi:10.1007/PL00013738.

——, P. van Rensch, T. Cowan, and A. Sullivan, 2010: Asymmetry in ENSO teleconnection with regional rainfall, its multidecadal variability, and impact. *J. Climate,* **23,** 4944–4955, doi:10.1175/2010JCLI3501.1.

Catto, J. L., N. Nicholls, and C. Jakob, 2012: North Australian sea surface temperatures and the El Nino–Southern Oscillation in the CMIP5 models. *J. Climate,* **25,** 6375–6382, doi:10.1175/JCLI-D-12-00214.1.

Chen, M., P. Xie, J. E. Janowiak, and P. A. Arkin, 2002: Global land precipitation: A 50-yr monthly analysis based on gauge observations. *J. Hydrometeor.,* **3,** 249–266, doi:10.1175/1525-7541(2002)003<0249:GLPAYM>2.0.CO;2.

Chen, W., H. F. Graf, and R. Huang, 2000: The interannual variability of East Asian winter monsoon and its relation to the summer monsoon. *Adv. Atmos. Sci.,* **17,** 48–60, doi:10.1007/s00376-000-0042-5.

——, J. Feng, and R. Wu, 2013: Roles of ENSO and PDO in the link of the East Asian winter monsoon to the following summer monsoon. *J. Climate,* **26,** 622–635, doi:10.1175/JCLI-D-12-00021.1.

Feng, J., L. Wang, W. Chen, S. K. Fong, and K. C. Leong, 2010: Different impacts of two types of Pacific Ocean warming on Southeast Asian rainfall during boreal winter. *J. Geophys. Res.,* **115,** D24122, doi:10.1029/2010JD014761.

——, W. Chen, C. Y. Tam, and W. Zhou, 2011: Different impacts of El Niño and El Niño Modoki on China rainfall in the decaying phases. *Int. J. Climatol.,* **31,** 2091–2101, doi:10.1002/joc.2217.

——, L. Wang, and W. Chen, 2014: How does the East Asian summer monsoon behave in the decaying phase of El Niño during different PDO phases? *J. Climate,* **27,** 2682–2698, doi:10.1175/JCLI-D-13-00015.1.

Gong, H., L. Wang, W. Chen, R. Wu, K. Wei, and X. Cui, 2014: The climatology and interannual variability of the East Asian winter monsoon in CMIP5 models. *J. Climate,* **27,** 1659–1678, doi:10.1175/JCLI-D-13-00039.1.

Horel, J. D., and J. M. Wallace, 1981: Planetary-scale atmospheric phenomena associated with the Southern Oscillation. *Mon. Wea. Rev.,* **109,** 813–829, doi:10.1175/1520-0493(1981)109<0813:PSAPAW>2.0.CO;2.

Huang, R., and Y. Wu, 1989: The influence of ENSO on the summer climate change in China and its mechanism. *Adv. Atmos. Sci.,* **6,** 21–32, doi:10.1007/BF02656915.

——, J. Chen, L. Wang, and Z. Lin, 2012: Characteristics, processes, and causes of the spatio-temporal variabilities of the East Asian monsoon system. *Adv. Atmos. Sci.,* **29,** 910–942, doi:10.1007/s00376-012-2015-x.

Huffman, G. J., R. F. Adler, D. T. Bolvin, and G. J. Gu, 2009: Improving the global precipitation record: GPCP version 2.1. *Geophys. Res. Lett.,* **36,** L17808, doi:10.1029/2009GL040000.

Hurwitz, M., N. Calvo, C. I. Garfinkel, A. H. Butler, S. Ineson, C. Cagnazzo, E. Manzini, and C. Peña-Ortiz, 2014: Extratropical atmospheric response to ENSO in the CMIP5 models. *Climate Dyn.,* **43,** 3367–3376, doi:10.1007/s00382-014-2110-z.

Jeong, H.-I., and Coauthors, 2012: Assessment of the APCC coupled MME suite in predicting the distinctive climate impacts of two flavors of ENSO during boreal winter. *Climate Dyn.,* **39,** 475–493, doi:10.1007/s00382-012-1359-3.

Ji, L., S. Sun, K. Arpe, and L. Bengtsson, 1997: Model study on the interannual variability of Asian winter monsoon and its influence. *Adv. Atmos. Sci.,* **14,** 1–22, doi:10.1007/s00376-997-0039-4.

Jiang, X., S. Yang, Y. Li, A. Kumar, W. Wang, and Z. Gao, 2013: Dynamical prediction of the East Asian winter monsoon by the NCEP Climate Forecast System. *J. Geophys. Res. Atmos.,* **118,** 1312–1328, doi:10.1002/jgrd.50193.

Kim, S. T., W. Cai, F.-F. Jin, and J.-Y. Yu, 2014: ENSO stability in coupled climate models and its association with mean state. *Climate Dyn.,* **42,** 3313–3321, doi:10.1007/s00382-013-1833-6.

Lau, N.-C., and M. J. Nath, 1996: The role of the ''atmospheric bridge'' in linking tropical Pacific ENSO events to extratropical SST anomalies. *J. Climate,* **9,** 2036–2057, doi:10.1175/1520-0442(1996)009<2036:TROTBI>2.0.CO;2.

Lee, J.-Y., and B. Wang, 2014: Future change of global monsoon in the CMIP5. *Climate Dyn.,* **42,** 101–119, doi:10.1007/s00382-012-1564-0.

——, ——, Q. Ding, K.-J. Ha, J.-B. Ahn, A. Kumar, B. Stern, and O. Alves, 2011: How predictable is the Northern Hemisphere summer upper-tropospheric circulation? *Climate Dyn.,* **37,** 1189–1203, doi:10.1007/s00382-010-0909-9.

——, S.-S. Lee, B. Wang, K.-J. Ha, and J.-G. Jhun, 2013: Seasonal prediction and predictability of the Asian winter temperature variability. *Climate Dyn.,* **41,** 573–587, doi:10.1007/s00382-012-1588-5.

——, B. Wang, K.-H. Seo, J.-S. Kug, Y.-S. Choi, Y. Kosaka, and K.-J. Ha, 2014: Future change of Northern Hemisphere summer tropical–extratropical teleconnection in CMIP5 models. *J. Climate,* **27,** 3643–3664, doi:10.1175/JCLI-D-13-00261.1.

Lee, S.-S., J.-Y. Lee, K.-J. Ha, B. Wang, and J. Schemm, 2011: Deficiencies and possibilities for long-lead coupled climate prediction of the western North Pacific–East Asian summer monsoon. *Climate Dyn.,* **36,** 1173–1188, doi:10.1007/s00382-010-0832-0.

Lee, T., D. E. Waliser, J.-L. F. Li, F. W. Landerer, and M. M. Gierach, 2013: Evaluation of CMIP3 and CMIP5 wind stress climatology using satellite measurements and atmospheric reanalysis products. *J. Climate,* **26,** 5810–5826, doi:10.1175/JCLI-D-12-00591.1.

Li, C., 1990: Interaction between anomalous winter monsoon in East Asia and El Niño events. *Adv. Atmos. Sci.,* **7,** 36–46, doi:10.1007/BF02919166.

Li, G., and S.-P. Xie, 2014: Tropical biases in CMIP5 multimodel ensemble: The excessive equatorial Pacific cold tongue and double ITCZ problems. *J. Climate,* **27,** 1765–1780, doi:10.1175/JCLI-D-13-00337.1.

Li, Y., and N.-C. Lau, 2012: Impact of ENSO on the atmospheric variability over the North Atlantic in late winter—Role of transient eddies. *J. Climate,* **25,** 320–342, doi:10.1175/JCLI-D-11-00037.1.

Magnusson, L., M. Alonso-Balmaseda, and F. Molteni, 2013: On the dependence of ENSO simulation on the coupled model mean state. *Climate Dyn.,* **41,** 1509–1525, doi:10.1007/s00382-012-1574-y.

Power, S., T. Casey, C. Folland, A. Colman, and V. Mehta, 1999: Inter-decadal modulation of the impact of ENSO on Australia. *Climate Dyn.,* **15,** 319–324, doi:10.1007/s003820050284.

Rasmusson, E. M., and T. H. Carpenter, 1982: Variations in tropical sea surface temperature and surface wind fields associated with the Southern Oscillation/El Niño. *Mon. Wea. Rev.,* **110,** 354–384, doi:10.1175/1520-0493(1982)110<0354:VITSST>2.0.CO;2.

Smith, T. M., R. W. Reynolds, T. C. Peterson, and J. Lawrimore, 2008: Improvements to NOAA's historical merged land–ocean surface temperature analysis (1880–2006). *J. Climate,* **21,** 2283–2296, doi:10.1175/2007JCLI2100.1.

Taschetto, A. S., A. Sen Gupta, N. C. Jourdain, A. Santoso, C. C. Ummenhofer, and M. H. England, 2014: Cold tongue and warm pool ENSO events in CMIP5: Mean state and future projections. *J. Climate,* **27,** 2861–2885, doi:10.1175/JCLI-D-13-00437.1.

Taylor, K. E., R. J. Stouffer, and G. A. Meehl, 2012: An overview of CMIP5 and the experiment design. *Bull. Amer. Meteor. Soc.,* **93,** 485–498, doi:10.1175/BAMS-D-11-00094.1.

Trenberth, K. E., G. W. Branstator, D. Karoly, A. Kumar, N.-C. Lau, and C. Ropelewski, 1998: Progress during TOGA in understanding and modeling global teleconnections associated with tropical sea surface temperatures. *J. Geophys. Res.,* **103,** 14 291–14 324, doi:10.1029/97JC01444.

Uppala, S. M., and Coauthors, 2005: The ERA-40 Re-Analysis. *Quart. J. Roy. Meteor. Soc.,* **131,** 2961–3012, doi:10.1256/qj.04.176.

Wang, B., R. Wu, and X. Fu, 2000: Pacific–East Asian teleconnection: How does ENSO affect East Asian climate? *J. Climate,* **13,** 1517–1536, doi:10.1175/1520-0442(2000)013<1517:PEATHD>2.0.CO;2.

——, ——, and T. Li, 2003: Atmosphere–warm ocean interaction and its impacts on Asian–Australian monsoon variation. *J. Climate,* **16,** 1195–1211, doi:10.1175/1520-0442(2003)16<1195:AOIAII>2.0.CO;2.

Wang, L., and W. Chen, 2010: How well do existing indices measure the strength of the East Asian winter monsoon? *Adv. Atmos. Sci.,* **27,** 855–870, doi:10.1007/s00376-009-9094-3.

——, and J. Feng, 2011: Two major modes of the wintertime precipitation over China. *Chin. J. Atmos. Sci.,* **35,** 1105–1116.

——, and W. Chen, 2014: An intensity index for the East Asian winter monsoon. *J. Climate,* **27,** 2361–2374, doi:10.1175/JCLI-D-13-00086.1.

Watanabe, M., and F.-F. Jin, 2002: Role of Indian Ocean warming in the development of Philippine Sea anticyclone during ENSO. *Geophys. Res. Lett.,* **29,** doi:10.1029/2001GL014318.

Weare, B., 2013: El Niño teleconnections in CMIP5 models. *Climate Dyn.,* **41,** 2165–2177, doi:10.1007/s00382-012-1537-3.

Webster, P. J., and S. Yang, 1992: Monsoon and ENSO: Selectively interactive systems. *Quart. J. Roy. Meteor. Soc.,* **118,** 877–926, doi:10.1002/qj.49711850705.

Weller, E., and W. Cai, 2013: Asymmetry in the IOD and ENSO teleconnection in a CMIP5 model ensemble and its relevance to regional rainfall. *J. Climate,* **26,** 5139–5149, doi:10.1175/JCLI-D-12-00789.1.

Wu, B., T. J. Zhou, and T. Li, 2009: Contrast of rainfall–SST relationships in the western North Pacific between the ENSO developing and decaying summers. *J. Climate,* **22,** 4398–4405, doi:10.1175/2009JCLI2648.1.

Xie, P., and P. A. Arkin, 1997: Global precipitation: A 17-year monthly analysis based on gauge observations, satellite estimates, and numerical model outputs. *Bull. Amer. Meteor. Soc.,* **78,** 2539–2558, doi:10.1175/1520-0477(1997)078<2539:GPAYMA>2.0.CO;2.

Xie, S.-P., K. Hu, J. Hafner, H. Tokinaga, Y. Du, G. Huang, and T. Sampe, 2009: Indian Ocean capacitor effect on Indo–western Pacific climate during the summer following El Niño. *J. Climate,* **22,** 730–747, doi:10.1175/2008JCLI2544.1.

Yang, X., and T. DelSole, 2012: Systematic comparison of ENSO teleconnection patterns between models and observations. *J. Climate,* **25,** 425–446, doi:10.1175/JCLI-D-11-00175.1.

Yuan, Y., and S. Yang, 2012: Impacts of different types of El Niño on the East Asian climate: Focus on ENSO cycles. *J. Climate,* **25,** 7702–7722, doi:10.1175/JCLI-D-11-00576.1.

Zhang, R., and A. Sumi, 2002: Moisture circulation over East Asia during El Niño episode in northern winter, spring and autumn. *J. Meteor. Soc. Japan,* **80,** 213–227, doi:10.2151/jmsj.80.213.

——, ——, and M. Kimoto, 1996: Impact of El Nino on the East Asian monsoon: A diagnostic study of the '86/87 and '91/92 events. *J. Meteor. Soc. Japan,* **74,** 49–62.

——, T. Li, M. Wen, and L. Liu, 2015: Role of intraseasonal oscillation in asymmetric impacts of El Niño and La Niña on the rainfall over southern China in boreal winter. *Climate Dyn.,* doi:10.1007/s00382-014-2207-4, in press.

Zhang, T., and D.-Z. Sun, 2014: ENSO asymmetry in CMIP5 models. *J. Climate,* **27,** 4070–4093, doi:10.1175/JCLI-D-13-00454.1.

Zhang, W., and F.-F. Jin, 2012: Improvements in the CMIP5 simulations of ENSO-SSTA meridional width. *Geophys. Res. Lett.,* **39,** L23704, doi:10.1029/2012GL053588.

——, ——, J.-X. Zhao, and J. Li, 2013: On the bias in simulated ENSO SSTA meridional widths of CMIP3 models. *J. Climate,* **26,** 3173–3186, doi:10.1175/JCLI-D-12-00347.1.

Zhu, J., B. Huang, Z.-Z. Hu, J. Kinter III, and L. Marx, 2013: Predicting US summer precipitation using NCEP Climate Forecast System version 2 initialized by multiple ocean analyses. *Climate Dyn.,* **41,** 1941–1954, doi:10.1007/s00382-013-1785-x.